Journal of Solid State Chemistry 183 (2010) 1670–1677

Contents lists available at ScienceDirect

Journal of Solid State Chemistry

journal homepage: www.elsevier.com/locate/jssc

p-Type thermoelectric properties of the oxygen-deficient perovskite $Ca_2Fe_2O_5$ in the brownmillerite structure

Emily Asenath-Smith, Indunil N. Lokuhewa, Scott T. Misture, Doreen D. Edwards *

Alfred University, Kazuo Inamori School of Engineering, 2 Pine Street, Alfred, NY 14802, USA

ARTICLE INFO

Article history:
Received 3 February 2010
Received in revised form
11 May 2010
Accepted 17 May 2010
Available online 20 May 2010

Keywords:
Calcium ferrite
Brownmillerite
Thermopower
Seebeck coefficient
Thermal properties
Electrical conductivity
Disproportionation

ABSTRACT

Brownmillerite calcium ferrite was synthesized in air at 1573 K and thermoelectric properties (direct current electrical conductivity σ, Seebeck coefficient α, thermal conductivity κ, thermal expansion α_L) were measured from 373 to 1050 K in air. Seebeck coefficient was positive over all temperatures indicating conduction by holes, and electrical properties were continuous through the *Pnma–Imma* phase transition. Based on the thermopower and conductivity activation energies as well as estimated mobility, polaron hopping conduction was found to dominate charge transport. The low electrical conductivity, <1 S/cm, limits the power factor ($\alpha^2\sigma$), and thus the figure of merit for thermoelectric applications. The thermal conductivity values of $\sim$2 W/mK and their similarity to Ruddlesden–Popper phase implies the potential of the alternating tetrahedral and octahedral layers to limit phonon propagation through brownmillerite structures. Bulk linear coefficient of thermal expansion ($\sim 14\times10^{-6}\,K^{-1}$) was calculated from volume data based on high-temperature *in situ* X-ray powder diffraction, and shows the greatest expansion perpendicular to the alternating layers.

© 2010 Elsevier Inc. All rights reserved.

1. Introduction

The ongoing investigation of oxide ceramics for thermoelectric applications seeks to support alternative energy power generation from excess heat: solar and geothermal heat sources, or waste heat from factories and automobiles, by incorporating oxide materials for their increased thermal and chemical stability. The actual efficiency of a thermoelectric material is proportional to a dimensionless figure of merit given by $ZT=\alpha^2\sigma T/\kappa$, where α is the Seebeck coefficient also known as thermopower, σ is the electrical conductivity, and κ the total thermal conductivity ($\kappa=\kappa_{el}+\kappa_{ph}$), which is a sum of the lattice (phonon) and electronic contributions. Target values include: $\kappa<1$ W/mK, $\sigma>10$ S/cm, $\alpha>150$ μV/K, with the goal of designing oxide materials that exhibit $ZT>1$ to compete with traditional intermetallic thermoelectrics [1]. These values illustrate the fundamental requirements of thermoelectric materials: simultaneous occurrence of high electrical conductivity and Seebeck coefficient, with low thermal conductivity. Ultimately it has been realized that thermoelectric materials must behave as a crystal electronically, and a glass thermally [2].

The voltage output by a thermoelectric pair (essentially a thermocouple) is maximized for materials with Seebeck coefficients that are similar functions of temperature [3]. Likewise, thermal expansion behavior of thermoelectric materials must be considered as these oxides will be paired not just with other semiconducting oxides, but also with metal electrode and oxide substrate materials. Thermomechanical failure has been encountered in oxide thermoelectric devices, and attributed to poor thermal expansion compatibility between oxides and metal electrodes [4,5]. Accordingly, oxide/silver composites are being explored for their ability to narrow the gap between the thermal expansion of oxides and silver electrodes [6]. The aforementioned requirements restrict the number of optimal combinations of thermoelements, and support the development of an assortment of *p*- and *n*-type oxides. *p*-Type systems based on cobalt oxide continue to drive the development of thermoelectric oxides since the discovery of lucrative thermoelectric properties in $NaCo_2O_4$ [7–10].

Compounds with the brownmillerite structure ($A_2B_2O_5$) are named after the brownmillerite mineral [11] (Ca_2AlFeO_5), which is a perovskite-derivative structure resulting from ordered oxygen vacancies and/or reduction of the *B*-site cation from a IV oxidation state to III according to:

$$2ABO_3 \rightarrow 2B'_B + V_O^{\bullet\bullet} + \frac{1}{2}O_2(g) + 5O_O^{\times} + 2A_A^{\times} \quad (1)$$

The (1/6) oxygen vacancies order in the [101] direction of the perovskite unit cell, introducing a fraction of tetrahedrally coordinated *B*-site cations, which alternate in a stacking sequence with octahedrally coordinated *B*-site cations along the *b*-axis (Fig. 1). The possibility of right- and left-handed orientations of

* Corresponding author. Fax: +1 607 871 2354.
E-mail address: dedwards@alfred.edu (D.D. Edwards).

0022-4596/$ - see front matter © 2010 Elsevier Inc. All rights reserved.
doi:10.1016/j.jssc.2010.05.016

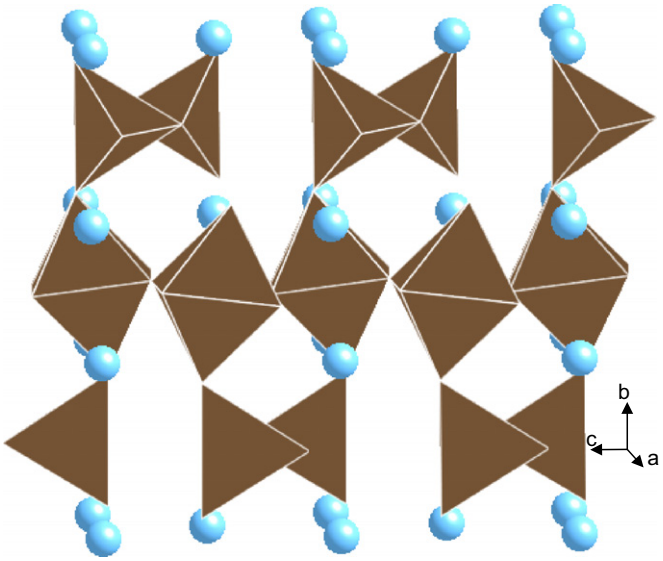

Fig. 1. Brownmillerite phase $Ca_2Fe_2O_5$, space group *Pnma*, showing alternating left- and right-handed tetrahedral chains. Light blue atoms represent Ca^{2+} ions, polyhedra represent Fe^{3+} ions, oxygen ions have been omitted for clarity.

the tetrahedra introduces polymorphic structures [12]. First, the low temperature phase, space group *Pnma* (*Pcmn*, number 62), contains alternating right- and left-handed configurations of tetrahedral chains. Depending on composition, two high temperature phases may exist: space group *I*2*mb* [13] containing tetrahedra that are all oriented in the same direction, and space group *Imma* [12], a phase with an aperiodic sequence of the tetrahedral chains [13,14]. Consistent with this view, a (3+1)-dimensional superspace group (*Imma*(00γ)*s*00) has been proposed [15] and recently confirmed in the $Ca_2Fe_2O_5$ composition [16]. Lastly, some brownmillerite structures may disorder at high temperatures [17] to form an oxygen-deficient cubic perovskite phase, marked by a shift in charge transport [18,19].

In general brownmillerite structures accommodate oxygen interstitials, charge compensated by holes, to exhibit *p*-type conduction according to:

$$\frac{1}{2}O_2(g) \Leftrightarrow O''_i + 2h^{\bullet} \quad (2)$$

where in iron-containing compounds the holes may be associated with Fe^{3+} cations, forming small polarons, to essentially produce a fraction of Fe^{4+} cations

$$Fe^{3+} + h^{\bullet} \rightarrow Fe^{4+} \quad (3)$$

with a resulting stoichiometry described as $Ca_2Fe_2O_{5+\delta}$ [20,21]. Loss of oxygen can be viewed as restoring stoichiometry by reducing Fe cations from the (IV) to (III) state. Finally, these structures are known to exhibit Jahn–Teller distortions, not due to the electronic nature of the constituent ions, but rather due to the existence of corner-shared octahedra and tetrahedra and their different inherent bond lengths which serve to trap charge carriers forming small polarons [22] and slowing charge transport [18].

The compound $Ca_2Fe_2O_5$ (mineral name srebrodolskite) is an antiferromagnetic mineral that crystallizes in the brownmillerite structure (space group *Pnma* shown in Fig. 1). It is characterized by a Néel temperature of ~720 K [13], and a congruent melting point of 1722 K [23]. Additionally, $Ca_2Fe_2O_5$ undergoes a phase transition from *Pnma* [16] (*Pcmn*) [24,25] to *Icmm* [25] (*I*2*mb* [24], *Imma*(00γ)*s*00 [16]) at ~950 K. This transition occurs over a 25 K temperature range, where both the low temperature and high temperature phases coexist [16]. The antiferromagnetic configuration of the Fe^{3+} ions in this structure is a result of *super-exchange* through intermediate oxygen anions to increase the covalency of the Fe–O bonds, while the variable valence of Fe cations serve to facilitate charge transport by hopping [26,27]. Mössbauer studies have confirmed the high-spin state of Fe cations in the brownmillerite structure for both octahedral and tetrahedral sites [13], which results in electronic structure $(t_{2g})^3(e_g)^2$ with half-filled levels in both tetrahedral and octahedral coordination.

$Ca_2Fe_2O_5$ has been studied for oxygen ionic transport [20,22] and its applications to Li-ion batteries [28] and catalysis [29–31]. An investigation of the room temperature elastic properties of $Ca_2Fe_2O_5$ have found oxygen vacancies to decrease bulk modulus and increase anisotropy of compression as compared to stoichiometric calcium perovskites [32]. Studies to apply compounds with the brownmillerite structure to thermoelectric systems are limited. Kobayashi et al. developed a brownmillerite type compound ($Ca_{2-y}La_yCo_{2-x}Al_xO_5$) for *n*-type thermoelectrics, and observed *p*-type behavior above 500 K, but deemed the thermoelectric properties inadequate due to the high resistivity [33]. Zhou and Goodenough [21] used thermopower measurements to study the electronic behavior of Fe^{3+}/Fe^{4+} calcium perovskites at low temperatures and report *n*-type behavior of $Ca_2Fe_2O_{5.16}$ below 300 K, with the Seebeck coefficient approaching positive values near 300 K.

Layered oxide structures have been used to achieve minimal thermal conductivity through increased phonon scattering introduced by the interfacial regions between layers. Due to the layered nature of brownmillerite structures, the potential of the octahedral–tetrahedral interfaces to reduce thermal conductivity through phonon scattering exists. Kobayashi et al. [33] found transport within the layers was 100 times higher than perpendicular to the layers, thus pointing to the potential of the layers to scatter phonons. However, in bulk polycrystalline materials, this anisotropy will certainly be averaged, which may limit the overall effect that the layers have to decrease thermal conductivity in bulk samples.

Due to the stringent thermal, electrical, and mechanical requirements on thermoelectric materials, an increase in the repertoire of *p*-type materials is advantageous to the realization of oxide thermoelectric devices. Herein we report on the thermoelectric properties of the brownmillerite compound $Ca_2Fe_2O_5$ prepared and analyzed in air for its application as a *p*-type thermoelectric material. The goal of this study is to expand the possible compositions of *p*-type thermoelectric materials to include those composed of materials with low toxicity, high natural abundance, and improved thermomechanical properties.

2. Experimental

2.1. Synthesis

Samples of $Ca_2Fe_2O_5$ were prepared using solid-state synthesis techniques. Stoichiometric proportions of $CaCO_3$ (Alpha Aesar, 99.9%) and Fe_2O_3 (Aldrich, 99.9%) were hand mixed in an agate mortar and pestle with isopropanol additions as necessary to facilitate mixing. After drying, powders were sieved to $<30\,\mu m$ and ~2.0 g portions were pressed uniaxially to ~12 MPa using a Carver Model M die press. The pressed pellets were calcined in air at 1272 K (10 K/min, 12 h), followed by reprocessing and reaction firing to 1373 K. Sintered compacts were formed as described above, followed by additional cold isostatic pressing to ~140 MPa. Samples were then sintered to 1573 K (10 K/min, 12 h) in air. Final densities of sintered compacts were >90% theoretical ($4.035\,g\,cm^{-3}$, calculated from refined lattice parameters), as found by the Archimedes method (ASTM Standard C 373-88).

2.2. Phase stability and microstructural analysis

Product powders were analyzed by X-ray powder diffraction at room temperature using a Phillips PW-1710 X-ray diffractometer equipped with Cu$K\alpha$ radiation. Finely ground sample powder was scanned from 10 to 80°2θ (1°2θ/min). High-temperature *in situ* X-ray powder diffraction was conducted on a customized Siemens θ–θ D500 X-ray diffractometer [34] equipped with Co$K\alpha$ radiation with product powders assembled in a thin layer on a Pt-coated sapphire disc, and heated from room temperature to 1623 K (30 K/min) and scanned from 20 to 80°2θ (4°2θ/min). Phase analysis was conducted using Jade 9 software (Materials Data Inc., USA), while lattice cell parameters were found from full pattern decomposition using TOPAS software (Bruker AXS, Germany). Thermogravimetric analysis (TGA) was conducted in air from 600 to 1673 K using an STA 449C simultaneous TGA-DTA measurement system (NETZSCH Instruments, Germany). Microstructural images were taken with an Amray 1810 scanning electron microscope at 18 kV, using thermally etched (1473 K, 1 h) fracture surfaces.

2.3. Thermoelectric characterization

Sintered compacts were cut into $\sim 4 \times 4 \times 12\ mm^3$ bars for electrical and thermopower characterization. Seebeck coefficient (thermopower) and direct current electrical measurements were made simultaneously using a custom made computer-controlled system that includes a current source (Model 2400 Keithley Instruments, Inc., USA) and a digital multi-meter (Model 2700, Keithely Instruments, Inc., USA) based on the four-point steady state gradient technique [35]. Thermal gradient was obtained by placing the sample off-center in a tube furnace, which allowed for $\sim$10 K temperature gradient along the length of the sample. Four type-R thermocouples (Pt/Pt–13%Rh) were attached to the gold-electroded sample bars by pressing with two gold foil plates at the bar ends and wrapping the remaining two thermocouples with gold wire to equidistant inner points on the bar. Seebeck coefficient was found from linear regression of ΔV vs. ΔT plot with corrections made for the platinum thermocouple leads. Reported values are the average of a minimum of 20 complete measurements taken at each temperature with standard deviations < 5 μV/K, and calculated error $< 10\%$ of reported values for $T < 500$ K and $< 3\%$ for $T > 500$ K. Multiple complete experiments were used to verify reproducibility. Direct current reversal technique was used to account for thermal emf. Electrical conductivity values reported are the average of a minimum of 20 measurements taken at each temperature, with standard deviations $< 1\%$ of the averages.

2.4. Thermal analysis

Linear coefficient of thermal expansion was calculated from high-temperature X-ray powder diffraction lattice parameter temperature dependence. Thermal conductivity was calculated from thermal diffusivity and specific heat measurements, which were found simultaneously using a Flashline 4010 laser-flash thermal diffusivity system (Anter Corporation, USA) along with bulk density.

3. Results

3.1. Phase and structural analysis

Brownmillerite phases of $Ca_2Fe_2O_5$ were obtained by solid-state reactions conducted at 1373 K in air consistent with Kanamaru et al. [36] and confirmed to be orthorhombic *Pnma* (JCPDS #00-018-0286) by X-ray powder diffraction (not shown). A darkening of the sample from brown to black was observed after sintering to 1573 K, with a slight decrease in lattice parameters as shown in Table 1.

Thermogravimetric analysis (TGA) and differential thermal analysis (DTA), shown in Fig. 2, were used to understand the stability range of product powders and to guide sintering parameters. Endotherms at $\sim$717 and $\sim$958 K confirmed the Néel temperature and the high temperature phase transition, respectively, while a gradual weight gain of 0.2% was observed up to 1400 K. A broad exotherm at 1423 K was associated with a $\sim$0.5% weight loss and accompanied the darkening of sample powders. Product powders obtained by reaction at 1373 K did not recover the lost weight upon cooling, while those samples sintered at 1573 K showed reversibility in the weight loss.

Fig. 3 shows results of high temperature *in situ* X-ray powder diffraction (up to 1623 K) used to probe for a structural evolution associated with the reduction of $Ca_2Fe_2O_5$ product powders (weight loss observed with TGA) at 1423 K. Results confirmed the high temperature phase transition, manifest in the disappearance of (131) and (151) peaks (34.1, 44.7°2θ, respectively) between 600 and 700 K [13,24]. The brownmillerite phase was maintained over all temperatures up to 1623 K, with no major structural rearrangements observed at the weight loss temperature 1423 K. The existence of a incommensurately modulated phase, characterized by the appearance of additional reflections ($h+k+l \neq 2n$) at high temperature was not investigated, as this phase transition has already been studied extensively by others [14,16]. The high temperature powder diffraction patterns were confirmed to orthorhombic *Ibmm* (JCPDS #01-089-8666, No. 74) after Berastegui et al. [25]. Based on introductory remarks, the phase transition in our system is believed to be the *Pnma*–*Imma*(00γ)*s*00 transition described by Krüger et al. but was not confirmed in the present study. The high temperature phase reported herein shall

Table 1
Room temperature lattice parameters of $Ca_2Fe_2O_5$ product powders after reaction (1373 K) and after sintering (1573 K).

Processing temperature	1373 K (Å)	1573 K (Å)
a	5.4257(3)	5.4219(4)
b	14.7638(9)	14.7521(14)
c	5.5953(3)	5.5947(5)

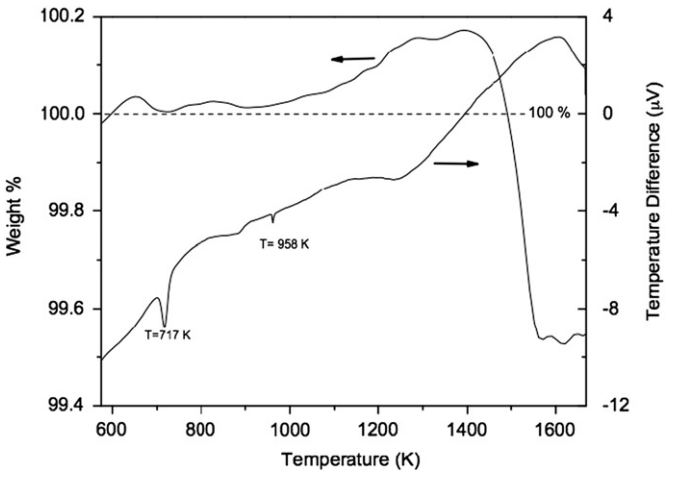

Fig. 2. Thermogravimetric analysis (TGA) and differential thermal analysis curves product powders preheated (sintered) to 1573 K.

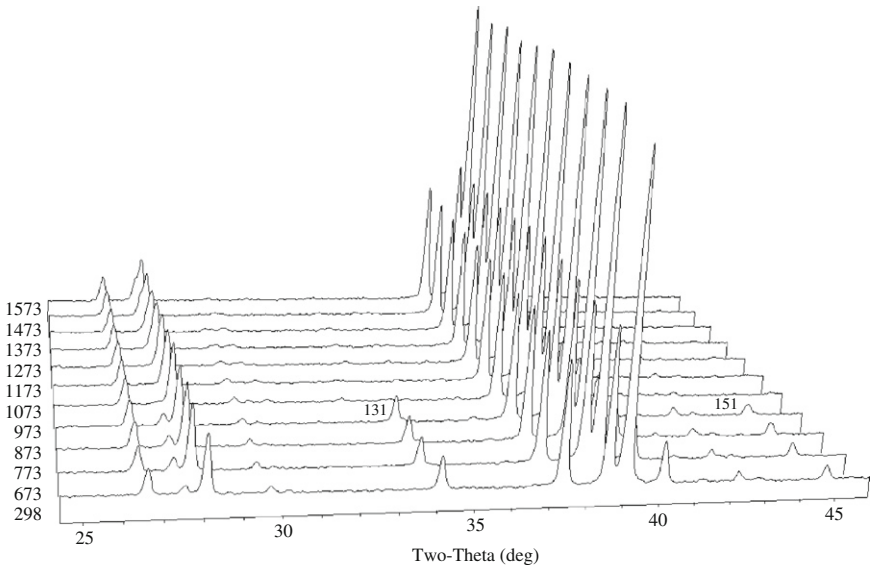

Fig. 3. High temperature *in situ* X-ray powder diffraction of $Ca_2Fe_2O_5$ product powders, taken every 100 K from 673 to 1573 K with room temperature pattern included. The *Pnma–Imma* phase transition at ~950 K is most notably evidenced by the disappearance of the 1 3 1 and 1 5 1 peaks.

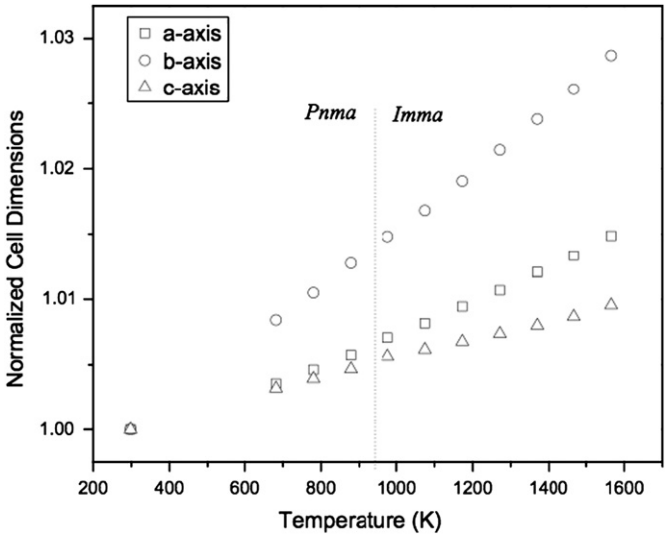

Fig. 4. Normalized cell dimensions of $Ca_2Fe_2O_5$ product powders refined from high-temperature X-ray diffraction data. Error bars are smaller than data points and not shown.

be referred to as the average orthorhombic *Imma* (No. 74) consistent with [14]. Upon cooling, the (131) and (151) peaks returned confirming the reversibility of the *Pnma* to *Imma* transition (not shown).

The temperature evolution of lattice parameters (normalized) are shown in Fig. 4, illustrating predominate thermal expansion in the *b*-direction consistent with previously published results [13,24,25]. The *Pnma–Imma* transition is labeled for clarity.

3.2. Direct current electrical conductivity and Seebeck coefficient

Based on phase and stability results, product powders were sintered at 1573 K, achieving >90% density. A representative microstructure of sintered compacts is shown in Fig. 5. Fig. 6 illustrates the Seebeck coefficient and DC electrical conductivity taken over the range of 373–1050 K. Seebeck coefficient values of $Ca_2Fe_2O_5$ samples are positive over all temperatures studied indicating hole-type conduction. Seebeck coefficient is seen to

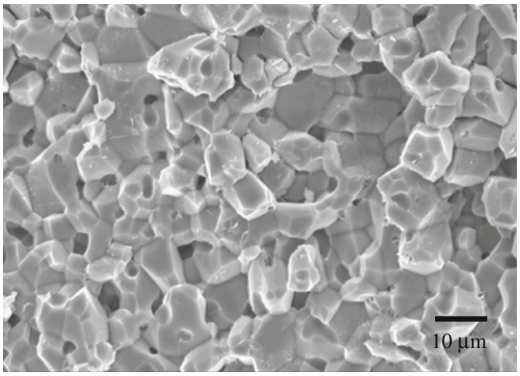

Fig. 5. Representative microstructure of $Ca_2Fe_2O_5$ samples used for thermoelectrical measurements (sintered at 1573 K, with >90% bulk density).

decrease with increasing temperature, while electrical conductivity increased with temperature, but remained <1 S/cm over all temperatures studied. Arrenhius plots of electrical conductivity were used to find activation energy for conduction (E_σ), consistent with a polaron conduction model based on [18]

$$\sigma T = \sigma_o \exp\left(\frac{E_\sigma}{k_B T}\right) \tag{6}$$

Likewise, a thermopower activation energy (E_α) was found from Seebeck coefficient data using Eq. (7), and represents the energy for carrier generation, as the Seebeck coefficient is measured in the absence of a current ($i=0$).

$$\alpha = \frac{k_B}{e}\left(\frac{E_\alpha}{k_B T} + \frac{S_v}{k_B}\right) \tag{7}$$

A comparison of the activation energies derived from each data set provides insight into the conduction mechanism. Activation energies that are equal ($E_\alpha = E_\sigma$) indicate the absence of a temperature-activated mobility, thereby implying a band conduction mechanism of charge transport, where $E_\alpha = E_\sigma$ is the energy associated with carrier generation only. Conversely, $E_\alpha < E_\sigma$ illustrates a temperature-activated mobility consistent with polaron conduction, where $E_\sigma - E_\alpha$ represents binding energy of the polaron [37]. Further, if the Seebeck coefficient, (α) plotted versus $1/T$ according to Eq. (7), does not show a temperature

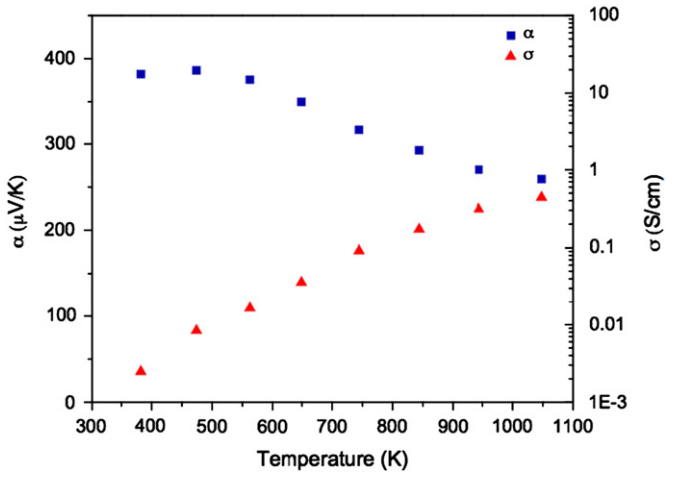

Fig. 6. DC conductivity and Seebeck coefficient of $Ca_2Fe_2O_5$ in air.

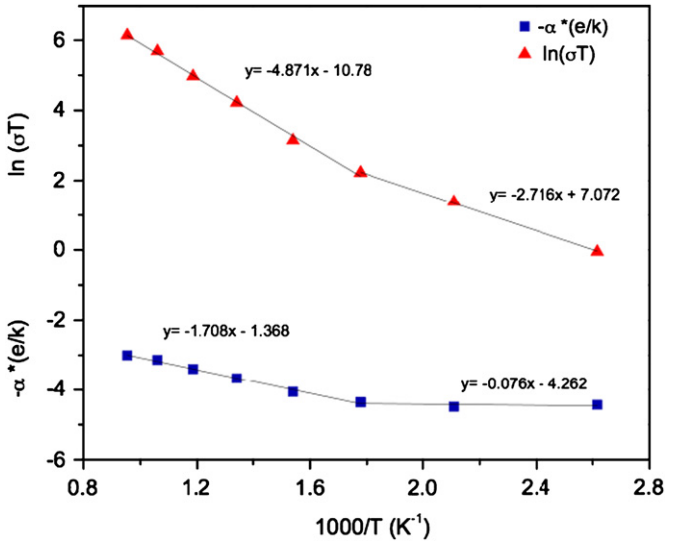

Fig. 7. Arrenhius plots used to find activation energies for thermopower and electrical conduction.

dependence, thereby maintaining a constant value, and $kT > E_\alpha$, a polaron transport mechanism is additionally supported and Eq. (8) can be used to model the observed behavior [38]

$$\alpha = \pm\left(\frac{k_B}{e}\right)\left[\ln\left(\frac{1-c}{\beta_p c}\right)+\frac{S_v}{k_B}\right] \tag{8}$$

In Eq. (8), β_p is a spin orbital degeneracy factor for p-type conduction, c is the fraction of Fe^{4+} sites (sites occupied by a hole carrier), and S_v is the vibrational (transport) entropy of the polaron. Often, S_v/k_B is neglected, as it is estimated to contribute only 10 μV/K [39]. When $\beta_p = 1$, Eq. (8) is known as the Heikes formula [40]. This formula is consistent with the diffusion-like characteristics of polaron transport which illustrates the restriction that a hole can only hop to an unoccupied site.

Fig. 7 was constructed using the relations shown in Eqs. (6) and (7), and the corresponding activation energies compiled in Table 2 were found from the slopes determined by linear regression of the data. Two distinct regions of behavior are seen, each with different activation energies and seemingly different conduction mechanisms. The temperature at which the conduction behavior transitions (~560 K) does not correspond to the Néel temperature (717 K), *Pnma–Imma* transition (~958 K), or the reduction at high temperature observed with TGA (~1423 K).

3.3. Thermal conductivity and thermal expansion

Thermal conductivity as a function of temperature is shown in Fig. 8. The discontinuity at ~700 K displays a correlation to the Néel transition (717 K) [41], while the slight change in behavior above ~950 K may be due to the emergence of the *Imma* phase at 958 K. Linear thermal expansion coefficients were found from X-ray powder diffraction data (Fig. 4) using:

$$\alpha_L = \frac{1}{L_o}\left(\frac{dL}{dT}\right) \tag{9}$$

Consistent with the *Pnma–Imma* transition, the coefficients of linear expansion were calculated for each phase separately and compiled in Table 3.

4. Discussion

The weight changes observed with TGA are attributed to oxygen exchange with the surrounding atmosphere, and a

Table 2
Activation energies for electrical conduction (E_σ) and thermopower (E_α) used to elucidate the conduction mechanism of $Ca_2Fe_2O_5$.

Activation energy	(i) $T < 560$ K (eV)	(ii) $T > 560$ K (eV)
E_σ	0.23	0.42
E_α	0.007	0.15
$E_\sigma - E_\alpha$	0.23	0.27

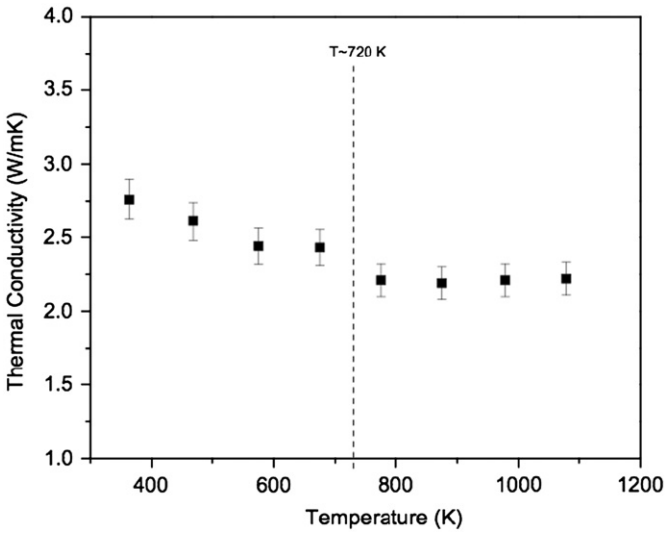

Fig. 8. Thermal conductivity of $Ca_2Fe_2O_5$ samples sintered at 1573 K. The discontinuity at ~720 K is attributed to the Néel transition.

Table 3
Linear coefficient of thermal expansion for $Ca_2Fe_2O_5$ calculated from high temperature X-ray powder diffraction data.

Unit cell direction	α_L ($\times 10^{-6}$ K^{-1})	
	Pnma (373–950 K)	*Imma* (950–1050 K)
a	9.8(3)	13.1(3)
b	21.9(3)	23.3(4)
c	8.1(3)	6.5(3)

corresponding change in the oxidation state of Fe cations consistent with introductory remarks. Increasing oxygen content serves to increase hole concentration (oxidation state of Fe), while weight loss (loss of oxygen content) will be associated with a decrease in charge carriers due to the loss of charge compensating holes. The preference of the brownmillerite structure to expansion in the *b*-direction illustrates the ability of these structures to accommodate excess oxygen between octahedral and tetrahedral layers: either in oxygen vacancies or in true interstitial sites.

4.1. Low temperature behavior ($373 < T < 560$ K)

Considerations of the conduction type, as elucidated by Seebeck coefficient measurements, and brownmillerite structural information can lead to an assessment of the defect relationships that underlie the electronic conduction mechanism in the $Ca_2Fe_2O_5$ system at low temperatures. The hole-type conduction can be explained by the presence of oxygen interstitials according to Eq. (2), where the holes can easily associate with Fe cations due to their variable oxidation states, forming polarons, consistent with Eq. (3), to yield an overall relationship of

$$Ca_2Fe_2O_5 + \frac{1}{2}O_2(g) \rightarrow 2(Fe^{3+} + h^{\bullet}) + O''_i + 2Ca^{\times}_{Ca} + 5O^{\times}_{O} \quad (10)$$

At temperatures below 560 K, Seebeck coefficient shows negligible temperature dependence ($E_{\alpha}=0.007$ eV, Fig. 6), while the electrical conductivity shows temperature dependence with activation energy 0.23 eV. This behavior indicates an activated mobility, consistent with polaron conduction mechanism of hole transport. Additionally, the binding energy of the polaron, E_{σ}–E_{α}, is consistent with similar values observed in other oxide systems [42]. This conduction mechanism is consistent with charge transport by holes, which hop between Fe^{3+} ions thereby introducing a fraction of Fe^{4+} ions during the association of the hole with an iron cation.

In this region, where charge conduction is facilitated by a polaron mechanism, Eq. (8) was applied to the observed thermopower to estimate *c*, the fraction of Fe^{4+}, directly related to the concentration of charge carriers (*p*). Accordingly, *p* was used with electrical conductivity values to estimate the hole mobility (μ_p), using the relation $\sigma_p = pe\mu_p$, which should be < 0.1 cm^2/V s in the case of a *small* polaron [22,37], that is when the hole carriers are strongly associated with Fe^{3+} ions introducing a fraction of Fe^{4+} ions between hops. This approach was loosely applied ($\beta_p = 6/5$, $S_v/k_B = 0$ in Eq. (8)) and confirmed the mobility to remain below 10^{-4} cm^2/V s in this temperature region. The low mobility coupled with the temperature-activated characteristics of the mobility corroborate a small polaron hole conduction mechanism in the $Ca_2Fe_2O_5$ system between 373 and 560 K [39].

4.2. High temperature behavior ($560 < T < 1050$ K)

Phase stability results indicate that the *Pnma–Imma* phase transition at $\sim$950 K in $Ca_2Fe_2O_5$ is not associated with a loss of oxygen (Fe reduction), and should not have a deleterious effect upon the observed electrical conductivity or thermopower when heating through this temperature range. Conversely, at higher temperatures ($T > 1423$ K), 0.5% weight loss by oxygen should be associated with reduction of Fe IV–III, consistent with the findings of Shaula et al. [22]. Alternatively viewed, a loss of hole concentration is initially implied

$$2(Fe^{\times}_{Fe^{3+}} + h^{\bullet}) + O''_i \rightarrow \frac{1}{2}O_2(g) + 2Fe^{\times}_{Fe^{3+}} \quad (11)$$

where further reduction (loss of oxygen) can be charge compensated by electron defects, which can associate with Fe (III) ions forming polarons to introduce a fraction of Fe (II). Experimental limitations prevented conductivity measurements at temperatures above 1250 K, and the speculated decrease in conductivity at $T > 1423$ K followed by a shift to *n*-type behavior could not be observed.

The simultaneous decrease in Seebeck coefficient and increase electrical conductivity indicates an increasing carrier concentration in this high temperature region. TGA data (Fig. 2) illustrate weight $\sim$100% throughout this temperature range, indicating a fairly constant oxygen content, which does not support an increase in hole carriers in accordance with Eq. (2). In this same region, the Seebeck coefficient shows temperature dependence according to Eq. (7), with activation energy of 0.15 eV, thereby implying a band model of conduction, consistent with the increasing carrier content. The calculated activation energy for electrical conduction is found to be 0.42 eV, which is 0.27 eV higher than that found for thermopower activation, and points toward a temperature-activated mobility, consistent with a polaron conduction mechanism. This discrepancy can have two different sources, as discussed below.

First, a mixed-type conduction could be present due to sufficient thermal energy to enable oxygen ionic transport, which can increase the apparent number of carriers while polaron conduction characteristics are maintained. The increase in ionic transference numbers in $Ca_2Fe_2O_5$ with increasing temperature has been shown, although electronic (hole) conduction dominates due to the two-dimensional nature of the diffusion paths in brownmillerite structures [20]. In addition, the migration enthalpy for oxygen transport in brownmillerite oxides has been found to be > 1 eV, which is significantly larger than the activation energies reported herein [19].

Secondly, charge disproportionation ($2Fe^{3+} \rightarrow Fe^{4+} + Fe^{2+}$) can serve to increase the number of carriers in the absence of oxygen exchange with the surrounding atmosphere. Ignoring ionic effects and assuming that $\sigma_n \ll \sigma_p$, the Seebeck coefficient can be expressed as

$$\alpha = \frac{k_B}{e}\left[\frac{\sigma_p}{\sigma_t}\ln\left(\frac{[Fe^{3+}]}{\beta_p[Fe^{4+}]}\right) - \frac{\sigma_n}{\sigma_t}\ln\left(\frac{\beta_n[Fe^{3+}]}{[Fe^{2+}]}\right)\right] \cong \frac{k_B}{e}\left[\ln\left(\frac{5[Fe^{3+}]}{6[Fe^{4+}]}\right)\right] \quad (12)$$

consistent with Eq. (8), where $\beta_p = 6/5$ is appropriate for iron in its high spin state. Assuming that *n*-type carriers have very low mobility [43], charge disproportionation will decrease the number of iron sites participating in the charge transport process as well as change the $[Fe^{3+}]/[Fe^{4+}]$ ratio. Below 560 K, the concentration of $[Fe^{4+}]$ was calculated to be 0.0099 ± 0.0006 from Eq. (12) assuming that $[Fe^{2+}]$ is negligible in this region. The charge disproportionation necessary to account for the decrease in the measured Seebeck coefficient above 560 K was determined to range from $[Fe^{2+}] = 0.004$ at 560 K to $[Fe^{2+}] = 0.029$ at 1048 K. The associated increase in Fe^{4+} corresponds to an increase in *p*-type carriers from $\sim 1.8 \times 10^{26}$ m^{-3} below 560 K to 6.9×10^{26} m^{-3} at 1048 K. The mobility calculated for the highest temperature was 0.003 cm^2/V s, which continues to support a polaron hopping mechanism [44].

Fig. 9 shows the equilibrium constant for the charge disproportionation reaction as a function of inverse temperature above 600 K, plotted as follows:

$$\ln(K_{eq}) = \frac{-\Delta H}{R}\left(\frac{1}{T}\right) + \frac{\Delta S}{R} \quad (13)$$

which derives from the standard Gibbs free energy expression, $\Delta G^{o}_{rxn} = -RT\ln K_{eq}$. The enthalpy and entropy of the disproportionation reaction were determined to be 43 ± 6 kJ/mol (0.45 ± 0.06 eV) and -13 ± 6 J/mol K, respectively. The calculated

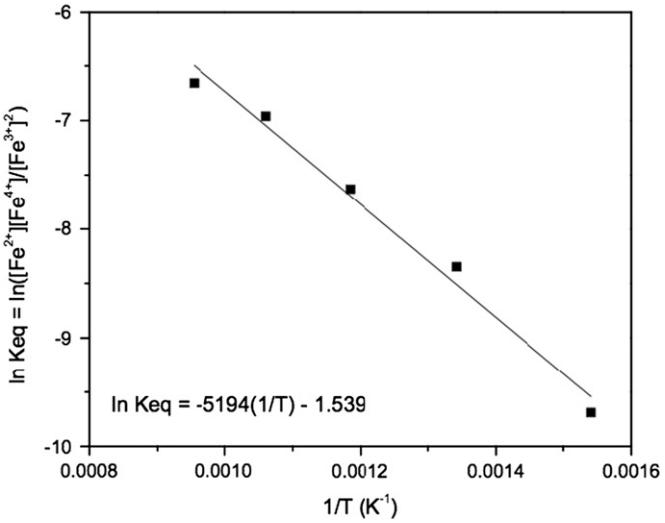

Fig. 9. Temperature dependence of charge disproportionation equilibrium constant calculated from measured thermopower data.

ΔH and ΔS values are not unreasonable compared to related materials [45,46]. For example, the enthalpy and entropy of Fe^{3+} charge disproportionation in the perovskite $La_{1-x}Sr_xFeO_3$ were reported to be $\sim$200 kJ/mol and $\sim$35 J/mol K, respectively. However, the extent of disproportionation is considerably lower for this material with $\ln K_{eq} = -16.5$ at 1173 K compared to -6.7 at 1048 K for $Ca_2Fe_2O_5$ [46].

The disproportionation of iron provides a plausible explanation for the temperature-activated generation of carriers. Additionally, the activation energy for mobility, with $E_\alpha - E_\sigma = 0.27$ eV, matches well with the polaron binding energy found for the low temperature region ($E_\alpha - E_\sigma = 0.23$ eV).

4.3. Thermal conductivity

Thermal conductivity values decreased from $\sim$3 to 2 W/mK over the entire temperature range studied (Fig. 8). The general target value for thermoelectric oxides, $\kappa < 1$ W/mK, has been satisfied in a large number of perovskite systems, which exhibit thermal conductivity values similar to [47] and lower [48] than those of $Ca_2Fe_2O_5$. The perovskite systems that exhibited considerably lower thermal conductivity were heavily substituted and thus served to benefit from point scattering of phonons in addition to any inherent structural scattering. In order to assess the ability of this undoped brownmillerite system to scatter phonons, the thermal conductivity of the undoped $CaFeO_3$ perovskite was considered. Thermal conductivity data for $CaFeO_3$ was compiled by Cheng et al. [49] for $T \leq 300$ K, and is reported to be $\sim$4.6 W/mK at 300 K. The lowest temperature at which the thermal conductivity of $Ca_2Fe_2O_5$ was measured in this study is $\sim$360 K, where $\kappa \sim 2.8$ W/mK. By extrapolating the $Ca_2Fe_2O_5$ data trend to $\sim$300 K, an estimated thermal conductivity of $\sim$3.0 W/mK at 300 K is found, thereby supporting the idea that the inherent browmillerite structural characteristics may facilitate further scattering of phonons over its perovskite counterpart.

The similarity of $Ca_2Fe_2O_5$ thermal conductivity values to the $n=2$ Ruddlesden–Popper phase of strontium titanate is noteworthy. The Ruddlesden–Popper phases show decreasing thermal conductivity over their perovskite counterparts. The $n=2$ phase shows thermal conductivity values decreasing from $\sim$4 to 2 W/mK over the temperature range 400–1050 K [50], which closely resembles the thermal conduction behavior of $Ca_2Fe_2O_5$ over the same temperature range. Thus, it may be the case that substituted brownmillerite structures can be made to exhibit minimal thermal conductivity values through the combined effect of doping and their layered structures.

4.4. Thermal expansion

A bulk linear thermal expansion coefficient was calculated using volume data before and after the *Pnma–Imma* transition and found to exhibit a small difference of 13.6×10^{-6} and 14.1×10^{-6} K^{-1}, respectively. These values can be considered representative of the behavior of a bulk polycrystalline sample due to the independence of thermal expansion on microstructure and porosity [51]. These values more closely resemble those of silver electrodes ($\sim 19 \times 10^{-6}\,K^{-1}$) than even the Ag/oxide composites ($12 \times 10^{-6}\,K^{-1}$), which were used to increase mechanical strength over the single phase oxide [5]. From the standpoint of thermal expansion alone, the linear thermal expansion coefficients of $Ca_2Fe_2O_5$ brownmillerite reported herein are an improvement over the Ag/oxide composites, and present increased compatibility with silver electrodes.

5. Conclusions

The thermoelectric properties of calcium ferrite ($Ca_2Fe_2O_5$) in the brownmillerite structure were measured in air from 373 to 1050 K and shown to exhibit *p*-type conduction. The hole carriers are charge compensation for oxygen interstitials and associate with Fe (III) cations to produce Fe (IV) cations and support a polaron conduction mechanism in this system. Charge disproportionation serves to increase carrier concentration above 560 K and was invoked to explain the temperature dependence of thermopower. The *Pnma–Imma* phase transition at 950 K is not associated with a loss of oxygen, and does not appear to affect thermoelectric behavior, as electrical conductivity and Seebeck coefficient are continuous over the range of 373–1050 K. The greatest thermal expansion occurs in the *b*-direction perpendicular to the alternating tetrahedral and octahedral layers, while the overall linear thermal expansion coefficient is found to be greater than similar single-phase perovskites. The direct application of $Ca_2Fe_2O_5$ as a *p*-type thermoelectric material is as yet limited by low electrical conductivity and thus low power factor ($\alpha^2\sigma$). Thermal conductivity is also high at >1 W/mK, but is similar to the undoped $n=2$ strontium titanate of the Ruddlesden–Popper homologous series, thereby supporting the potential of the layered regions of brownmillerite structures to suppress phonon transport. Aliovalent doping can serve to simultaneously increase electrical conductivity and decrease thermal conductivity, and may actually bring desirable ZT values to this brownmillerite system.

Acknowledgments

The authors are grateful to Swavek Zdzieszynski for his experimental assistance with high temperature X-ray diffraction facilities. Emily Asenath-Smith gratefully acknowledges the National Science Foundation Graduate Research Fellowship Program.

References

[1] T.M. Tritt, M.A. Subramanian, Mater. Res. Bull. 31 (3) (2006) 188–194.
[2] G.A. Slack, in: D.M. Rowe (Ed.), CRC Handbook of ThermoelectronicsCRC Press, Boca Raton, FL, 1995, pp. 407–440.
[3] D.D. Pollock, in: Thermoelectricity: Theory, Thermometry, ToolAmerican Society for Testing and Materials, Philadelphia, PA, 1985, pp. 111–132.

[4] I. Matsubara, R. Funahashi, T. Takeuchi, S. Sodeoka, T. Shimizu, K. Ueno, Appl. Phys. Lett. 78 (23) (2001) 3627–3629.
[5] A. Kosuga, S. Urata, K. Kurosaki, S. Yamanaka, R. Funahashi, Jpn. J. Appl. Phys. 47 (8) (2008) 6399–6403.
[6] S. Urata, R. Funahashi, T. Mihara, A. Kosuga, S. Sodeoka, T. Tanaka, Int. J. Appl. Ceram. Technol. 4 (6) (2007) 535–540.
[7] I. Terasaki, Physica B 383 (1) (2006) 107–110.
[8] I. Terasaki, Y. Sasago, K. Uchinokura, Phys. Rev. B 56 (20) (1997) R12685–R12687.
[9] K. Takahata, Y. Iguchi, D. Tanaka, T. Itoh, I. Terasaki, Phys. Rev. B 61 (19) (2000) 12 551–12 555.
[10] Y. Miyazaki, Solid State Ionics 172 (2004) 463–467.
[11] M. Data Brownmillerite, 〈http://www.mindat.org/min-790.html〉 (September 16, 2009).
[12] A.M. Abakumov, M.G. Rozova, E.V. Antipov, Russ. Chem. Rev. 73 (9) (2004) 847–860.
[13] G.J. Redhammer, G. Tippelt, G. Roth, R.G. Amthauer, Am. Mineral. 89 (2-3) (2004) 405–420.
[14] H. Krüger, V. Kahlenberg, Acta Crystallogr. B B61 (2005) 562–565.
[15] S. Lambert, H. Leligny, D. Grebille, D. Pelloquin, B. Raveau, Chem. Mater. 14 (4) (2002) 1818–1826.
[16] H. Krüger, V. Kahlenberg, V. Petříček, F. Phillipp, W. Wertl, J. Solid State Chem. 182 (6) (2009) 1515–1523.
[17] S.A. Speakman, J.W. Richardson, B.J. Mitchell, S.T. Misture, Solid State Ionics 149 (2002) 247–259.
[18] R.J.D. Tilley, in: Defects in SolidsJohn Wiley & Sons, Hoboken, NJ, 2008.
[19] G.B. Zhang, D.M. Smyth, Solid State Ionics 82 (3–4) (1995) 161–172.
[20] A.L. Shaula, Y.V. Pivak, J.C. Waerenborgh, P. Gaczyński, A.A. Yaremchenko, V.V. Kharton, Solid State Ionics 177 (33–34) (2006) 2923–2930.
[21] H.D. Zhou, J.B. Goodenough, J. Solid State Chem. 178 (12) (2005) 3679–3685.
[22] A.L. Shaula, V.V. Kharton, N.P. Vyshatko, E.V. Tsipis, M.V. Patrakeev, F.M.B. Marques, J.R. Frade, J. Eur. Ceram. Soc. 25 (4) (2005) 489–499.
[23] B. Phillips, A. Muan, J. Am. Ceram. Soc. 41 (11) (1958) 445–454.
[24] K. Fukuda, H. Ando, J. Am. Ceram. Soc. 85 (5) (2002) 1300–1302.
[25] P. Berastegui, S.-G. Eriksson, S. Hull, Mater. Res. Bull. 34 (2) (1999) 303–314.
[26] R.J.D. Tilley, in: Understanding Solids: The Science of MaterialsJohn Wiley & Sons, Chichester, England, 2004, pp. 363–390.
[27] A.R. West, in: Solid State Chemistry and its ApplicationsJohn Wiley & Sons, Chichester, England, 1984, pp. 553–582.
[28] N. Sharma, K.M. Shaju, G.V.S. Rao, B.V.R. Chowdari, Electrochim. Acta 49 (7) (2004) 1035–1043.
[29] Y. Yang, Z. Cao, Y. Jiang, L. Liu, Y. Sun, Mater. Sci. Eng. B 132 (3) (2006) 311–314.
[30] A. Kawashima, K. Matsubara, K. Honda, Bioresource Technol. 99 (9) (2008) 3439–3443.
[31] D. Hirabayashi, T. Yoshikawa, K. Mochizuki, S. Kazuhiro, K. Suzuki, Y. Sakai, Catal. Lett. 110 (3–4) (2006) 269–274.
[32] N. Ross, R. Angel, F. Seifert, Phys. Earth Planet. Int. 129 (1–2) (2002) 145–151.
[33] W. Kobayashi, A. Satake, I. Terasaki, Jpn. J. Appl. Phys. 41 (1) (2002) 3025–3028.
[34] S.T. Misture, Meas. Sci. Technol. 14 (2003) 1091–1098.
[35] A. Trestman-Matts, S.E. Dorris, T.O. Mason, J. Am. Ceram. Soc. 66 (8) (1983) 589–592.
[36] F. Kanamaru, H. Miyamoto, Y. Mimura, M. Koizumi, M. Shimada, S. Kume, S. Shin, Mater. Res. Bull. 5 (1970) 257–262.
[37] N.F. Mott, E.A. Davis, in: Electronic Processes in Non-crystalline Materials, Clarendon Press, Oxford, 1979.
[38] M.F. Hundley, J.J. Neumeier, Phys. Rev. B 55 (17) (1997) 511511 55 (1997) 5.
[39] H.L. Tuller, A.S. Nowick, J. Phys. Chem. Solids 38 (8) (1977) 859–867.
[40] R.R. Heikes, in: Thermoelectricity: Science and EngineeringInterscience Publishers, New York, 1961, pp. 77–82.
[41] C. Picard, P. Gerdanian, Solid State Commun. 87 (9) (1993) 775–778.
[42] N.F. Mott, in: Metal–Insulator TransitionsTaylor & Francis, London, 1974.
[43] M.V. Patrakeev, I.A. Leonidov, V.L. Kozhevnikov, K.R. Poeppelmeier, J. Solid State Chem. 178 (2005) 921–927.
[44] J.B. Goodenough, Prog. Solid State Chem. 5 (1971) 145–399.
[45] J. Mizusaki, T. Sasamoto, W.R. Cannon, H.K. Bowen, J. Am. Ceram. Soc. 66 (4) (1983) 247–252.
[46] M. Søgaard, P.V. Hendriksen, M. Mogensen, J. Solid State Chem. 180 (2007) 1489–1503.
[47] G. Xu, R. Funahashi, Q. Pu, G. Liu, R. Tao, G. Wang, Z. Ding, Solid State Ionics 171 (1–2) (2004) 147–151.
[48] K. Kobayashi, S. Yamaguchi, T. Tsunoda, Y. Imai, Solid State Ionics 144 (1–2) (2001) 123–132.
[49] J.-G. Cheng, J.-S. Zhou, J.A. Alonso, J.B. Goodenough, Y. Sui, K. Matsubayashi, Phys. Rev. B 80 (2009) 104430.
[50] K. Koumoto, I. Terasaki, R. Funahashi, Mater. Res. Bull. 31 (3) (2006) 206–210.
[51] R.W. Rice, in: Porosity of CeramicsMarcel Dekker, New York, 1998, p. 44.